Research paper

Sweeping water jet ring quenching of a large steel bar near industrial conditions

A.V.S. Oliveira [a] , D. Maréchal [b] , D. Lawrjaniec [c] , M. Gradeck [d],*

[a] GOTAS/LETeF, Mechanical Engineering Department, São Carlos School of Engineering, University of São Paulo, São Carlos, Brazil
[b] IRT M2P, 4 rue Augustin Fresnel 57070 Metz, France
[c] Ascometal CREAS, BP70045 Avenue de France, 57301 Hagondange, France
[d] Université de Lorraine, CNRS, LEMTA, F-54000 Nancy, France

ARTICLE INFO

ABSTRACT

Jet impingement cooling is a prevalent phenomenon in various industrial processes, particularly within metallurgy, and has garnered considerable attention in the literature. However, most investigations have been confined to laboratory-scale setups. This paper presents an experimental examination of steel bar cooling utilizing water jet ring that sweeps back and forth along the bar. Conducted under conditions closely resembling industrial settings, the tests involved a steel sample of substantial dimensions (80 mm in diameter and 1 m in length), subjected to an initial temperature near 900 °C, using a water ring comprised of 120 jets evenly distributed along five rows, and testing water flow rates ranging from 300 to 600 L/min (Re_j between 22,100 and 44,200). Employing a pseudo-analytical inverse method, the study aimed to estimate the boundary heat flux, surface temperature, and consequently, the heat transfer coefficient. Analysis of temperature measurements and estimated heat flux allowed to reveal key points into the cooling process: the onset of cooling, preceding the arrival of the jet ring; the maximum cooling rate, occurring in the impingement region; and the maximum heat flux, typically observed after the passage of the water jet ring. Excluding non-realistic points of the experiments, a correlation was established between the dissipated heat flux and surface temperature, as well as between the heat transfer coefficient and the surface temperature. Notably, neither the dissipated heat flux nor the heat transfer coefficient exhibited dependence on the position relative to the water ring location, indicating a sole dependency on surface temperature. In the tested conditions, the influence of water flow rate was found to be relatively little, confirmed through additional tests at flow rates of 300 L/min and 600 L/min. Temperature measurements at the bar center differed by only 2 °C after two minutes of cooling and six passes of the water jet ring, reaffirming the little effect of water flow rate in the tested condition. Finally, numerical simulations in production line conditions using the proposed correlation performed relatively well, slightly overestimating the bar exit temperature by about 80 °C, which is partially explained by the latent heat of transformation that was neglected in the inverse heat conduction model.

1. Introduction

Numerous engineering applications demand efficient cooling systems to manage high heat transfer rates, driving ongoing research activities. The necessity for robust heat dissipation arises from various needs: high power density devices, like microelectronics cooled by micro heat sinks [1] or refrigeration [2] (motivating innovative solutions to achieve high levels of heat dissipation [3,4]); safety reasons, like nuclear reactors in a hypothetical accidental condition [5,6]; or rapid cooling requirements, like in metallurgy to attain desired microstructural characteristics and mechanical properties of steels [7, 8].

The literature abounds with studies investigating fast cooling or quenching in metallurgical contexts, employing techniques like spray cooling, jet impingement, and others, encompassing both experimental and numerical investigations. However, most experimental studies are confined to laboratory scales and stationary flat surfaces, exemplified by works by Leocadio et al. [9] and Karwa and Stephan [10]. Some efforts have sought to replicate metal movement in actual production lines, such as the study by Gomez et al. [11] and Guemo et al. [12] utilizing a linear movement unit. Other studies have explored the effect of surface movement on heat dissipation using a rotating cylinder [13–15]. Jahedi and Moshfegh [16] investigated heat dissipation from

---

* Corresponding author.
E-mail address: michel.gradeck@univ-lorraine.fr (M. Gradeck).

Table 1

Experimental studies of hot metallic bar cooling with water jet impingement.

Authors	Year	Cylinder	Specimen material	Dimensions [mm] ($D \times L$ or $D \times L \times t$)	$T_{w,0}$ [°C]	T_j [°C]	N_j [-]	d_n or d_j [mm]	v_j [m/s]	Q [l/min]	$q''_{w,max}$ [MW/m^2]	$T_{w,rew}$ [°C]	v_{rew} [mm/s]	Δt_{rew} [s]
Agrawal et al.	2016	Full	SS-316	D12 × 300	800	24	1	⌀2.5–⌀4.8	–	–	2–17	750–800	1–20	0–25
Chabicovsky et al.	2015	Full	SS	D300	920	Room	32–48	–	0.02–0.75	–	1.2–3.5[a]	–	–	–
Devynck et al.	2016	Hollow	42CrMo4	D76 × 500 × 6	900	20	1 (planar)	2	0,9	–	1.8–2.8	650–850	–	–
Gradeck et al.	2009	Hollow	Ni-201	D175 × 200 × 37.5	500–600	17–90	1 (planar)	4	0.8–1.2	–	1–5	220–500	–	–
Jahedi and Moshfegh	2019	Hollow	Carbon steel	D96 × 173 × 16 D152 × 173 × 25 D192 × 173 × 32	250–600	15–55	1–2 rows[b]	⌀8	0.9–4.1	2.7–12.5	0.8–4.0	250–600	–	3–32
Mozumder et al.	2014	Hollow	SS-304	D135 × 150 × 10	460–560	20–40	1	⌀15	0.57–0.94	6–10	0.4–10	–	–	3–11
Present study	2024	Full	Carbon steel	D80 × 930	850–900	25	120	⌀2.7	7.3–14.6	100–600	1.5–2.5	–	38[c]	–

[a] These values were estimated from their results in terms of heat transfer coefficients.

[b] We understand from the figures that each row had three equally-spaced nozzles arranged along the cylinder axis.

[c] This value is the same as the water jet ring velocity, as we show in the results.

rotary hollow cylinders using arrays of jets, while Agrawal et al. [17] examined cooling of a vertically oriented cylindrical part impinged by a single water jet. Baghel et al. [18] conducted jet cooling experiments on a curved stainless steel foil, allowing evaluation of the Nusselt number through thermal imaging. However, most of these studies utilized nozzle sizes tailored for laboratory experimentation, potentially limiting the observation of large-scale characteristics of the material cooling, as noted in our previous study [19] focused on flat plate cooling.

To the best of our knowledge, the study closest to industrial conditions regarding jet cooling of cylindrical parts was conducted by a research group from Brno University of Technology. Chabicovsky et al. [20] developed an experimental facility capable of quenching tests on cylindrical parts, employing a jet ring containing 32 to 48 nozzles. Despite advancements, experimental data on cylinder quenching under industrial conditions remain scarce (some studies compiled in Table 1), prompting continued interest in numerical studies [21,22] to bridge this gap. Consequently, an experimental bench was constructed at IRT M2P (Metz, France) to conduct quenching experiments on plates and cylinders under conditions closely resembling industrial settings. Using this facility, in this paper, we present results from experiments involving a rotary carbon steel cylinder (35MnCrMoV5), quenched by a water jet ring composed of 120 nozzles sweeping back and forth along the sample length, with water volumetric flow rates ranging from 300 to 600 l/min. Our study aims to simulate the cooling process of a long cylindrical piece in a production line, offering insights into the kinetics of the cooling process and assessing the influence of water volumetric flow rate on sample cooling. We employed 15 thermocouples to measure material temperature during cooling, facilitating the estimation of dissipated heat flux through the corresponding inverse heat conduction problem. Our analysis unveils a correlation between wall heat flux and surface temperature, independent of water ring position, and evaluates the effect of water volumetric flow rate on sample cooling dynamics.

2. Experimental apparatus and test procedure

2.1. Test facility and instrumentation

The experimental setup utilized in this study, situated at IRT M2P as depicted in Fig. 1, is the facility employed in our previous investigation [19] focusing on single water jet cooling of a large nickel plate. With dimensions of approximately $7 \times 3 \times 5$ m^3, the installation comprises: (1) a cooling chamber, (2) a furnace, (3) a compressed air tank (2500 liters), and (4) a pre-heated water tank (2000 liters). This structure was designed to accommodate large-scale samples, such as plates measuring up to 1000 mm in length and 400 mm in width, as well as full or hollow bars with a maximum diameter of 100 mm. The water injection system can be configured as static, like in our previous study [19], or mobile, with velocities up to 600 mm/s, as

Fig. 1. Photograph of the large-scale cooling experimental bench: (1) cooling chamber; (2) furnace; (3) compressed air tank; (4) pre-heated water tank. [19].

implemented in the present investigation, featuring nozzles capable of generating jets or sprays. Up to 15 thermocouples can be used to measure the sample's temperature across various locations, facilitating the estimation of dissipated heat flux through an inverse method to solve the corresponding heat conduction problem. Although occasional disturbances from water droplets or steam may impede visualization, high-definition cameras installed inside the cooling chamber enable observation and recording of the experiments. The furnace operates within a controlled nitrogen environment, elevating the test sample to a temperature of 920 °C while mitigating surface oxidation. The compressed air tank interfaces with the controlled-temperature water tank, which, in turn, connects to the injection system. Thus, pressure serves as the controlled parameter for water injection.

Using the experimental setup described, we present the results of quenching experiments conducted on a large cylindrical steel piece (35MnCrMoV5[1]), measuring 80 mm in diameter and 930 mm in length. To emulate a production line, the cylinder underwent a slow rotation around its axis ($\omega = 5.7$ rpm). Fig. 2a illustrates the hydraulic circuit of the bench, encompassing the key components previously depicted

---

[1] This grade of steel is completely austenitic at 900 °C. Water quenching enables to form martensite when the temperature is below $M_s = 335$ °C for this grade, M_s being the temperature at which the martensitic transformation starts. In this grade, another transformation from austenite to bainite appears, but only for low enough cooling rates. For the considered geometry, the bainitic transformation may only affect the near-center of the steel bar.
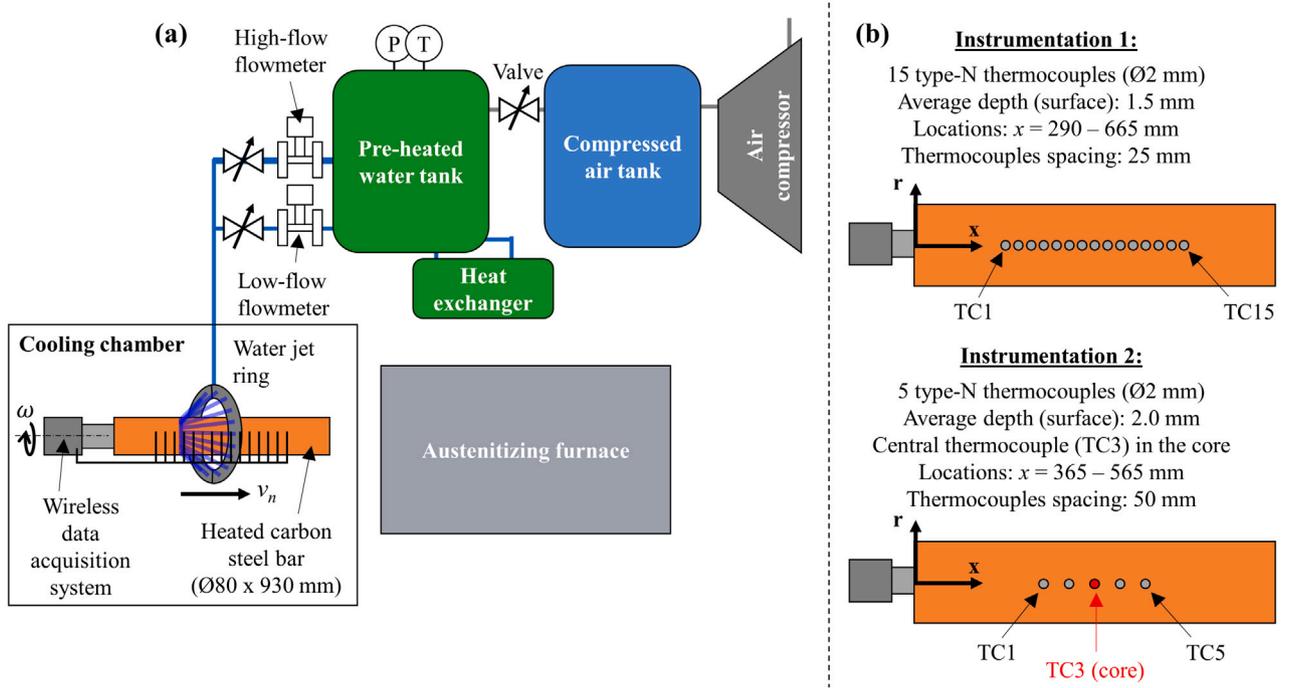
Fig. 2. Schematic drawing of the hydraulic circuit for the water injection.

in Fig. 1. Flowmeters, pressure transducers, and thermocouples were employed to respectively measure the flow rate, injection pressure, and liquid temperature throughout the cooling process. Given the high flow rates involved in this study, only the high-flow flowmeter was utilized, although an additional flowmeter for lower flow rates is available if required. Two types of instrumentation were employed (Fig. 2b): one to provide detailed estimates of the heat flux profile along the cylinder axis, and another to measure the core temperature, situated at the center of the sample. Both instrumentation setups utilized 2-mm type-N sheathed and ungrounded thermocouples. For the first instrumentation approach, 15 probes were inserted into the test sample, positioned radially and nearly traversing the entire product until reaching approximately 1.5 mm from the diametrically opposite side. In the second instrumentation setup, five thermocouples were employed, with the central thermocouple inserted to reach the sample axis, enabling measurement of the core temperature, while the remaining four thermocouples measured the sample temperature 2 mm below the surface. Throughout all experiments, temperature measurements were acquired at a sample rate of 50 Hz, providing detailed monitoring of the cooling process.

Quenching was promoted by a mobile system comprising 120 nozzles, equally spaced in the angular direction and arranged in five rows to form a water jet ring (length of the impinged region of 38 mm), directed towards the heated sample and sweeping it at a constant velocity of $v_n = 0.038$ m/s. The water jet was at ambient temperature, i.e. between 25 and 27 °C. Upon reaching the end position, the quenching system rapidly returned to the start point (without cutting the water injection) at a velocity of approximately 0.6 m/s, recommencing the sweeping motion at velocity v_n. This reciprocal movement aimed to emulate a production line scenario with multiple water jet rings. Despite the sample length of 930 mm, the effective sweeping length was approximately 700 mm, resulting in each quenching cycle lasting 18.4 s. The water jet impinged upon the sample at an angle of 30° from the cylinder axis, oriented in the opposite direction to the system's movement. The distance between the nozzles and the sample surface was approximately 28 mm.

Table 2

Experimental conditions for each test (the initial temperature uncertainty comprises the maximum and minimum temperature measurements).

Test	n° TCs	Q [l/min]	v_j [m/s]	Re_j [-]	We_j [-]	$T_{w,0}$ [°C]
1	15	300	7.3	22,100	1990	881 ± 5
2	15	450	10.9	33,100	4450	875 ± 6
3	15	600	14.6	44,200	7980	890 ± 5
4	5	300	7.3	22,100	1990	863 ± 5
5	5	600	14.6	44,200	7980	871 ± 2

2.2. Test conditions

In this study, we varied the water volumetric flow rate Q from 300 to 600 L/min, which resulted in a range of jet Reynolds numbers Re_j from 22,100 to 44,200, calculated using the following expression:

$$Re_j = \frac{v_j d_n}{\nu_j} \tag{1}$$

where v_j is the jet velocity (estimated assuming balanced flow rates among the 120 nozzles), ν_j is the kinematic viscosity of water at room temperature (0.893 mm²/s), and d_n is the diameter of the nozzle (2.7 mm). We also calculated the jet Weber number We_j, defined by:

$$We_j = \frac{\rho_j v_j^2 d_n}{\sigma_j} \tag{2}$$

where ρ_j and σ_j are, respectively, the water specific mass (998 kg/m³) and surface tension (0.072 N/m) at room temperature. These two numbers will be useful in the discussion of the results. Table 2 summarizes the experimental conditions of the present study: the number of thermocouples used in the test (n° TCs), the flow rate Q, the jet velocity v_j, the jet Reynolds number Re_j (Eq. (1)), the jet Weber number We_j (Eq. (2)) and the initial wall temperature $T_{w,0}$, whose value is the mean of all the thermocouples measurements (the uncertainty includes the maximum and the minimum temperature measurements).
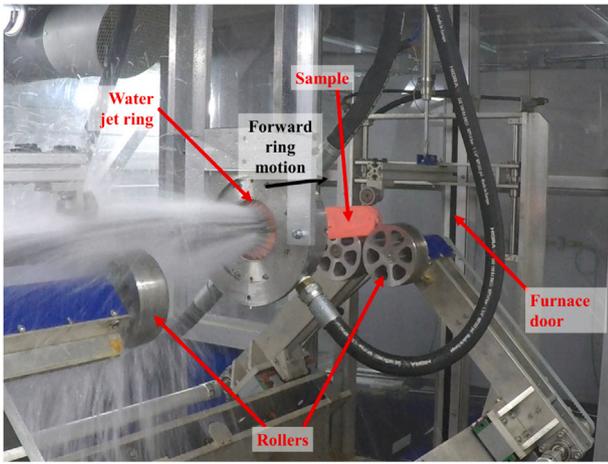
Fig. 3. Picture of a quenching test captured by the monitoring camera.

2.3. Test methodology

Several tests were performed in this experimental campaign, each sample being used twice or thrice only because, if more tests were conducted, cracks were observed near the extremity where we mounted the data acquisition system. We ensure test reproducibility during these three tests with the same sample. The test protocol employed in this study proceeded as follows:

1. The instrumented sample underwent heating within the furnace until reaching a temperature of 920 °C, maintaining this temperature for a duration of one hour;
2. Then, the injection pressure in the water line was adjusted. Once all experimental parameters stabilized, particularly the injection pressure and sample temperature, the monitoring camera started recording as the sample was extracted from the furnace using an automatic motion system. The sample was then positioned on four rollers to facilitate rotation during the cooling process;
3. Water injection started from a position that did not directly impact the sample, allowing the water flow to stabilize before initiating the cooling test. Meanwhile, the sample underwent initial cooling via natural convection and radiation, resulting in a minor temperature drop (approximately 30 to 50 °C, as indicated in Table 2);
4. Upon achieving the desired and stable test conditions, the jet ring started sweeping back and forth over the sample, as previously described. The test duration averaged about 2.5 min. Fig. 3 provides a visual representation of the experiment, showcasing various components mentioned in these steps.

3. Data reduction and uncertainty analysis

3.1. Heat flux estimation

To solve the inverse heat conduction problem, we could model our cylindrical sample as a two-dimensional axisymmetric body with thermally insulated surfaces at the extremities. In this case, considering constant thermophysical properties, the heat equation that would describe this problem is the following:

$$\frac{\partial^2 \theta}{\partial r^2} + \frac{1}{r}\frac{\partial \theta}{\partial r} + \frac{\partial^2 \theta}{\partial x^2} = \frac{1}{\alpha}\frac{\partial \theta}{\partial t} \tag{3}$$

where $\theta(x,t) = T(x,t) - T_0(x,0)$ is the difference between the temperature T and the body's initial temperature T_0, r is the radius, x the longitudinal position, t is the time and $\alpha = \lambda/(\rho c)$ is the material's thermal diffusivity, which is calculated using the thermal conductivity

Table 3
Thermophysical properties for 35MnCrMoV5 (austenitic phase).

T [°C]	λ [W m^{-1} K^{-1}]	ρ [kg m^{-3}]	c_p [J kg^{-1} K^{-1}]
300	40.6	7755	510
500	36.4	7683	544
700	31	7606	575
900	27.2	7574	606

λ, the specific mass ρ and the specific heat c of the material.

We must highlight that neglecting both the temperature- and phase-dependency of the steel thermophysical properties and the latent heat of phase transformation does not affect the quality of the heat flux estimate in fast cooling processes like quenching, as we demonstrated in a previous study [7]. For the material 35MnCrMoV5, due to phase transformations during quenching, the thermophysical properties can vary depending on the cooling rate. However, since this study focuses exclusively on quenching, we predominantly observe martensite formation near the surface at temperatures below the martensite start temperature ($M_s = 335$ °C for 35MnCrMoV5), while the core of the material remains in the austenitic phase. This simplifies the analysis, as the dependency of the material properties can be reduced to temperature only, allowing us to mainly consider the properties of the austenitic phase. Hence, Table 3 shows the thermophysical properties used for the heat flux estimation, which are averaged for temperatures between 500 and 900 °C. These values include: $\lambda = 32$ W m^{-1} K^{-1}, $\rho = 7650$ kg m^{-3}, $c_p = 570$ J kg^{-1} K^{-1}, which results in $\alpha = 7.34$ mm^2 s^{-1}. Although assuming constant properties is reasonable in this case, it is important to note that temperature- and phase-dependent properties can have a significant impact, especially if there are more pronounced variations in material properties with temperature or if the cooling rate is lower. Therefore, caution is required when extending this assumption to cases where such variations play a larger role.

However, the number of thermocouples utilized in this study fails to adequately capture sharp spatial gradients in the x-direction, consequently compromising the precision of the heat flux profile estimate. This limitation is elaborated upon in Appendix. Therefore, instead of solving the two-dimensional heat equation as presented in Eq. (3), as we did in a previous study involving flat plate cooling by a single jet [19], we opted to neglect axial heat conduction effects when formulating the inverse heat conduction problem. This one-dimensional assumption was validated through virtual simulations of the experiment Appendix. Consequently, for each thermocouple position along the x-direction, the heat equation simplifies to:

$$\frac{\partial^2 \theta}{\partial r^2} + \frac{1}{r}\frac{\partial \theta}{\partial r} = \frac{1}{\alpha}\frac{\partial \theta}{\partial t} \tag{4}$$

which becomes the following ordinary differential equation after applying the Laplace transform:

$$\frac{\partial^2 \overline{\theta}_n}{\partial r^2} + \frac{1}{r}\frac{\partial \overline{\theta}_n}{\partial r} - \frac{p}{a}\overline{\theta}_n = 0 \tag{5}$$

where p is Laplace variable and $(\overline{\cdot})$ correspond to a variable in Laplace space. Eq. (5) is a modified Bessel equation whose solution is:

$$\overline{\theta} = c_1 I_0\left(\sqrt{\frac{p}{\alpha}}r\right) + c_2 K_0\left(\sqrt{\frac{p}{\alpha}}r\right) \tag{6}$$

I and K being modified Bessel functions of the first and second kind ("0" is their order), respectively. Considering the boundary conditions of the problem (symmetry at $r = 0$ and dissipative heat flux $\varphi_w(x,t)$ at $r = R$, the cylinder radius), we find the particular solution of the problem in the Laplace space:

$$\overline{\theta} = -\frac{1}{\lambda}\frac{I_0\left(\sqrt{\frac{p}{\alpha}}r\right)}{\sqrt{\frac{p}{\alpha}}I_1\left(\sqrt{\frac{p}{\alpha}}R\right)}\overline{\varphi}_w \tag{7}$$

Using the convolution property of the Laplace transform [23], we can calculate the inverse transform and find the temperature difference θ in the real space as follows:

$$\theta(r,t) = -\frac{1}{\lambda} \int_0^t \varphi_w(t) Z(r, t-\tau) \, d\tau \qquad (8)$$

where Z is:

$$Z(r,t) = \mathcal{L}^{-1} \left[\frac{I_0\left(\sqrt{\frac{p}{\alpha}}r\right)}{\frac{p}{\alpha} I_1\left(\sqrt{\frac{p}{\alpha}}R\right)} \right] \qquad (9)$$

which is calculated in the present study using the Stehfest algorithm [24]. Using Duhamel's theorem by assuming constant heat flux by parts, Eq. (8) becomes the following summation:

$$\theta(r, t_k) = \sum_{m=0}^{k-1} X(r, t_k - t_m)\varphi_w(t_k) \qquad (10)$$

where:

$$X(r, t_k) = -\frac{1}{\lambda} \int_{t_k}^{t_{k+1}} Z(r, \tau) d\tau \qquad (11)$$

As this is an inverse problem, our objective is to estimate the heat flux over time $\varphi_w(t)$ for each thermocouple position along the x-direction, denoted by x_{TC}, utilizing temperature measurements. Eq. (10) outlines that theoretically, we could derive the transient heat flux $\varphi_w(t_k)$ from the sample temperature difference $\theta(t_k) = T(t_k) - T_0$ obtained through thermocouple measurements. The impulse response (Eq. (11)) is estimated utilizing material properties (specifically, α and λ), system geometry (cylinder radius R), and the radial position r of thermocouple measurements. However, the inverse problem is inherently ill-posed, needing a regularization method to mitigate the effect of measurement noise when estimating the dissipated heat flux. In this study, we employed Beck's function specification method [25], also known as the future time steps method, which involves filtering temperature measurements by assuming a functional form for future heat fluxes. Specifically, n_{fts} future temperature measurements are utilized to estimate the present heat flux, assuming knowledge of past heat fluxes and considering constant heat flux for the n_{fts} future time steps. This formulation yields a system of equations for estimating φ_w using the least squares method. The selection of n_{fts} demands careful consideration: choosing a value that is too small could yield highly noisy estimates of φ_w maybe even unreadable, while a value that is too large may behave like a low-pass filter, losing information during fast transients that is crucial in quenching studies. Using only $n_{fts} = 2$ future time steps, we obtained stable and high-quality heat flux estimates. It is noteworthy that with $n_{fts} = 1$, the heat flux estimate always diverges.

Although numerical solutions can be very useful for non-linear inverse heat conduction problems [26] or complex geometries, analytical and pseudo-analytical solutions are advantageous to provide fast results (provided a regular geometry), as its computational time is much shorter. While a numerical inversion can take a couple of minutes or a few hours, depending on the complexity of the problem, an analytical inversion takes only a dozen of seconds or a couple of minutes. Furthermore, as we show in Appendix, the solution for the 1D problem is the same as for the 2D problem for the fundamental Fourier harmonic ($\omega_n = 0$), which makes it very convenient when coding the inverse method.

3.2. Effect of the thermocouple response time

In a previous study [27], we introduced a method to correct thermocouple signals for the delay in temperature response, particularly relevant for applications aiming at heat flux estimation using an inverse method. Following the same procedure, we determined the thermocouple response time for our instrumentation, employing a sample composed of the same material and instrumented with two thermocouples. One thermocouple, identical to those used in the experiments, was inserted into the sample, while the other was a type-K thermocouple with a 0.25 mm diameter wire soldered to the sample, serving as a reference. This investigation yielded a response time of $t_c = 0.78 \pm 0.07$ s.

Notably, due to the larger thermocouple diameter utilized in the present study compared to the previous one (2 mm versus 1 mm, respectively), the response time is higher than the previously reported 0.35 s [27]. Despite this finding, indicating potentially more significant temperature correction, the temperature slope observed in the current results is considerably lower — only a few dozen degrees per second, compared to the previous tests where it could reach a few hundred degrees per second. Consequently, the impact of the thermocouple response time is minor in the present study. For instance, Fig. 4a displays the measured temperatures for selected thermocouples used in test 3, the highest water volumetric flow rate experiment. The filled lines represent the original temperatures, while the dashed lines represent the corrected temperatures considering the thermocouple response time. Although the original and corrected temperature plots look similar, differences at a given instant can exceed 50 °C when the cooling rate is high, which is a non-negligible discrepancy. However, despite these differences, the estimated heat fluxes remain highly consistent, with the largest difference being below 5%. Therefore, to ensure the best precision of our inverse method, we employed the thermocouple signal correction we proposed in [27], utilizing a response time of $t_c = 0.78$ s.

3.3. Detection of key points during the cooling

Using the temperature measurements and the estimated heat flux profile, we identified three distinct points, referred to as "key points," during the cooling process. Fig. 5 illustrates these key points detection using data from test 1:

- *Onset of Cooling (OoC)*: This denotes the point where the temperature measurement begins to decrease more significantly compared to previous instants. For the initial pass of the water ring, it means the point where the cooling rate surpasses that induced by free convection and radiation. Accordingly, this point is identified by progressively monitoring the average cooling rate along with its standard deviation, and identifying the point where the derivative in time (which is negative) falls below the average minus five times the standard deviation — i.e., a significant increase in the cooling rate. For subsequent water ring passes, it corresponds to the point where the temperature stops to recover at the thermocouple position (i.e., the temperature derivative in time becomes negative).
- *Maximum Cooling Rate (MCR)*: This marks the instant where the magnitude of the temperature derivative with respect to time is maximal, indicating the point of peak cooling rate. Detection involves identifying negative peaks in this temperature derivative.
- *Maximum Heat Flux (MHF)*: After the application of the inverse method and estimation of heat flux evolution at each thermocouple position, peaks in the heat flux for each water ring pass can be identified.

3.4. Parameters uncertainties

The measurement uncertainties in the present study are as follows: 1 °C for wall temperature, 0.5 L/min for water volumetric flow rate, and 0.1 mm for thermocouple positions. As done in a prior study [19], we found that our inverse method estimates the boundary heat flux with an accuracy of 0.2 MW/m^2 and the surface temperature with an accuracy of 2 °C, considering potential errors in thermocouple positions and thermophysical properties. Furthermore, regarding the key points,
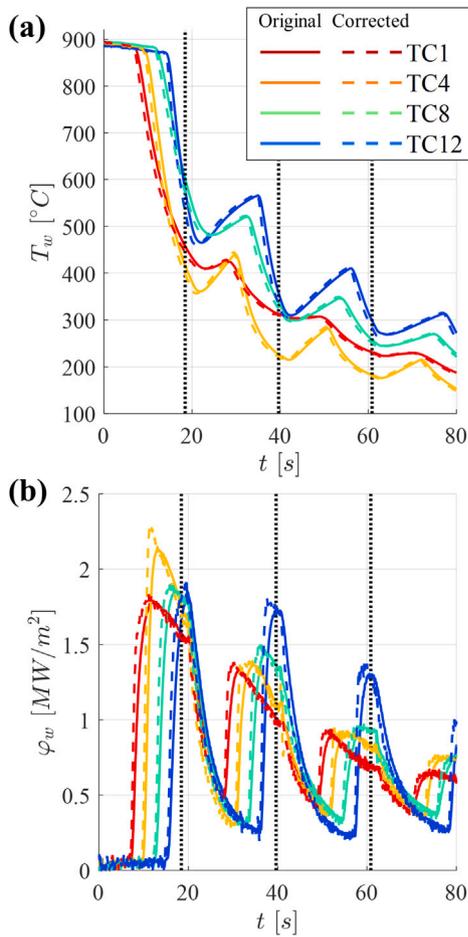
Fig. 4. Results of the thermocouple measurement correction based on its response time (test 3): (a) temperature evolution, comparing the original and corrected signals; (b) estimated heat fluxes using both the original and corrected signals. In the figures, TC stands for thermocouple.
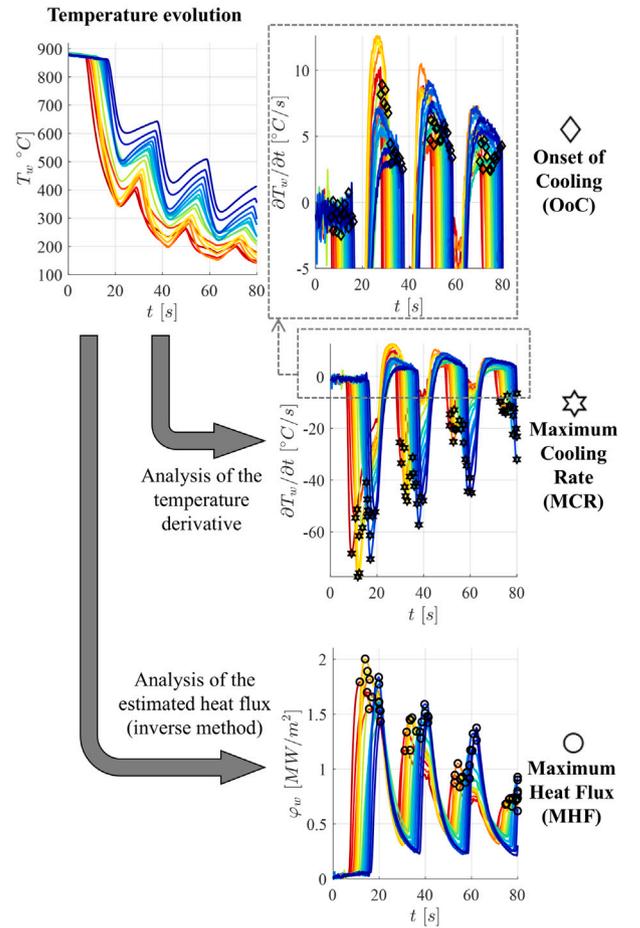

Fig. 5. Illustration of the method to detect each key point of the cooling process: OoC and MCR based on the temperature derivative and MHF based on the estimated heat flux.

positional uncertainty aligns with that of the thermocouple positions, approximately 0.1 mm, while temporal uncertainty corresponds to the acquisition period (20 ms). It is important to note that the MHF point detection may have a slight delay due to the inverse method, as regularization tends to damp rapid transients. However, in this study, such delays are minimal (less than 40 ms, according to validation results detailed in Appendix).

4. Results and discussion

In this section, we present the outcomes of our study. Initially, we meticulously examine the findings from test 1, beginning with a comprehensive discussion on the surface temperature estimate. Then, we explore the behavior of temperature, heat flux, and key points throughout the cooling process. For this initial analysis, we concentrate on the first 80 s of cooling to establish a correlation between wall heat flux and, consequently, the heat transfer coefficient, relative to surface temperature. Following this, we investigate the impact of water mass flow rate on the cooling process.

4.1. Detailed discussion of test 1 results

For heat transfer studies, it is important to present results in terms of surface temperature T_s rather than measured temperature T_w, especially when estimating the heat transfer coefficient. Due to the

intense heat transfer rate on the surface, a significant radial temperature gradient arises, leading to notable differences between these two temperatures. Fig. 6 presents, for selected thermocouples, the evolution of both measured (dashed lines) and estimated surface temperatures (filled lines). The vertical dotted black lines denote the instants when the ring completes its sweeping motion and returns to the starting point. Surface temperature was estimated by applying the heat flux derived from the inverse method in Eq. (10) for $r = R$. As anticipated, the surface temperature experiences a slight decline before and a more pronounced decrease compared to the measured temperature. Their disparity is not negligible, sometimes exceeding 50 °C. Consequently, all subsequent results presented in this paper regard only the recalculated surface temperature. Additionally, the zoomed-in section at the start of the cooling in the same figure showcases the accurate detection of the onset of cooling and maximum cooling rate. These methods for detecting key points appear to be valid for the other ring passes as well.

All the thermocouple measurements are now presented in Fig. 7 alongside the heat flux evolution estimated by the inverse method at each thermocouple position. During the water ring pass, there is a progressive cooling process, starting with TC1 and occurring thermocouple by thermocouple until reaching TC15, which means a rapid increase in the dissipated heat flux. When the water ring finishes its course, indicated by the vertical dotted black lines, there is a substantial temperature recovery due to heat conduction from the sample core taking place almost simultaneously for all the thermocouples. This results in a heat flux decrease that is virtually uniform over the surface, following a negative exponential decrease with a characteristic time of
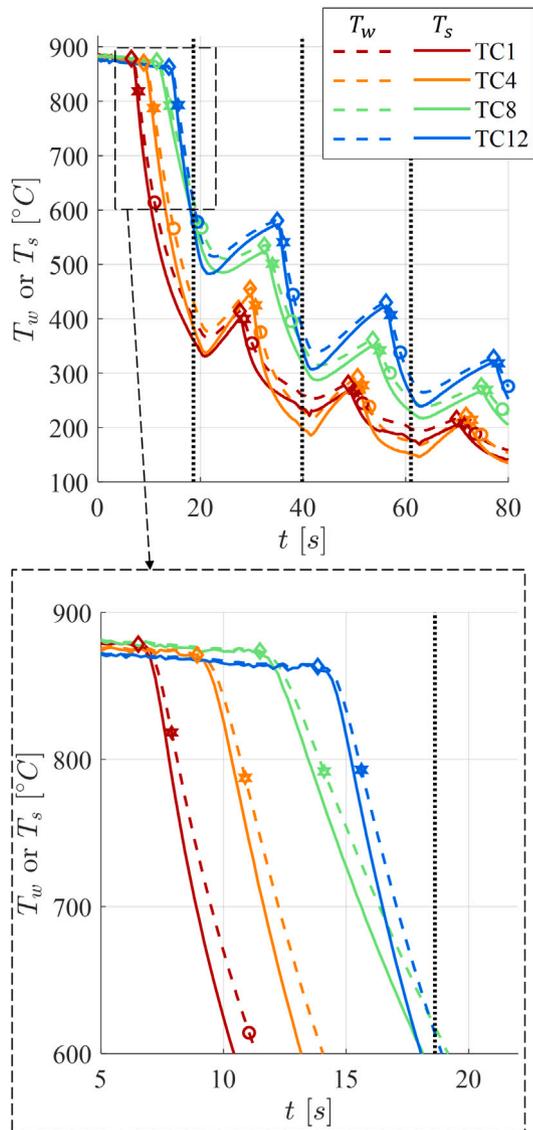
Fig. 6. Comparison between the measured temperature T_w and the estimated surface temperature T_s (test 1), including the detected key points (OoC: ◇, MCR: ✩; MHF: ○). Bottom graph is a zoom at the first moments of the cooling during the first ring pas.

Fig. 7. Test 1 results of surface temperature evolution (a) and estimated heat flux evolution (b), including the detected key points (OoC: ◇, MCR: ✩; MHF: ○) and the end of each ring pass (vertical dotted black lines). After the first ring pass, there is an exponential decay in the heat flux, represented by the dashed pink line.

$t_d = 7$ s (depicted by the dashed pink line in Fig. 7). Subsequently, the water ring passes over the thermocouples again, interrupting the temperature recovery and initiating another rapid cooling process until the end of the water ring course, restarting the exponential temperature decrease, and the cycle starts over again.

The results shown in Fig. 7 confirm the expected sequence of key points during the cooling process: the onset of cooling appears first in all the ring passes, followed by the maximum cooling rate, and eventually, the maximum heat flux. This sequence mirrors our observations from a previous study involving single jet cooling of a large plate [19]. It is worth noting that wall rewetting cannot occur at contact temperatures surpassing the thermodynamic limit of water superheat (approximately 330 °C at 1 bar [28]). Although the estimated contact surface temperature in the present results is around 750 °C (using classical solution of contact between two semi-infinite bodies [29]), apparently contradicting physical principles, it is essential to recognize that these are large-scale experiments employing inserted thermocouples for temperature measurements. Consequently, heat diffusion effects dampen fast transients occurring on the surface, especially at the surface roughness scale, where intense local cooling
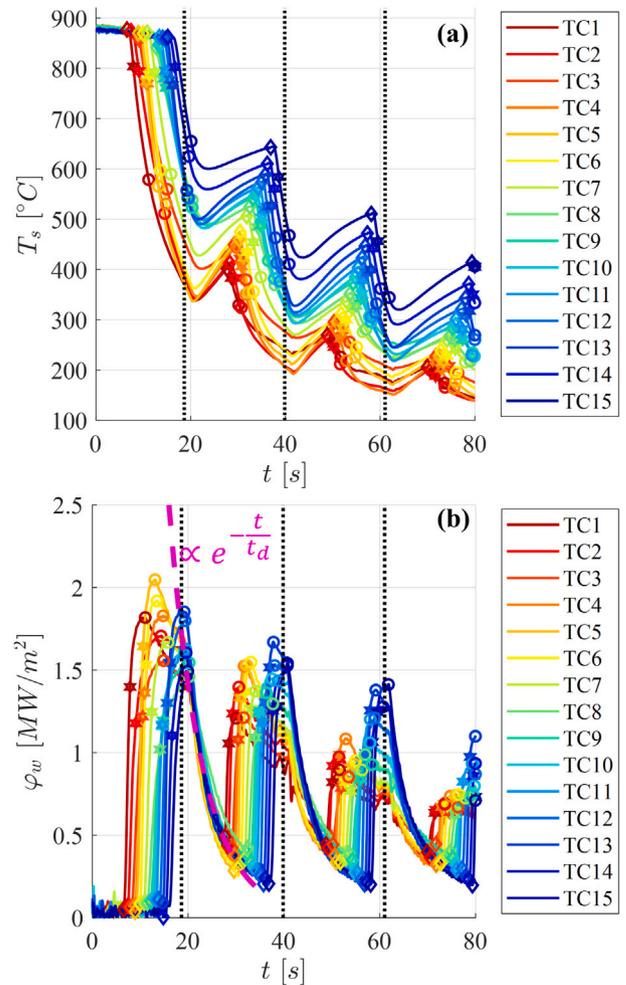
processes and subsequent wall rewetting occur [30], which may not be fully captured in experiments under industrial conditions. This analysis explains the reason behind our choice of labeling the first key point as the "onset of cooling" rather than "wall rewetting".

In Fig. 8, we compare the behavior of these key points relative to the water ring position, depicted by a green shaded region with the legend x_{imp}. It is important to remind that the water ring consists of five rows of jets, resulting in a 38-mm-thick impinged zone instead of a single impact location. For the first ring pass, when the steel is at a very high temperature and the surface is completely dry, we observe an almost linear progression of the onset of cooling and maximum cooling rate points, but not the maximum heat flux point. This discrepancy arises because the cooling is still in the Leidenfrost regime, significantly reducing heat dissipation until wall rewetting occurs. Consequently, the peak heat flux occurs towards the end of the first ring pass for thermocouples TC8 to TC15 – or, more accurately, when the water ring is returning to the initial position for the second sweep – while the dissipated heat flux is still increasing. In subsequent ring passes, all the key points advance linearly in time with the same slope as the water ring sweeping. Furthermore, after the first pass, the onset of cooling occurs slightly before the arrival of the water ring, which is a result of the axial heat conduction as the neighboring region is already being cooled by the jets. The maximum cooling rate occurs in the jet impingement region, and the maximum heat flux follows after the
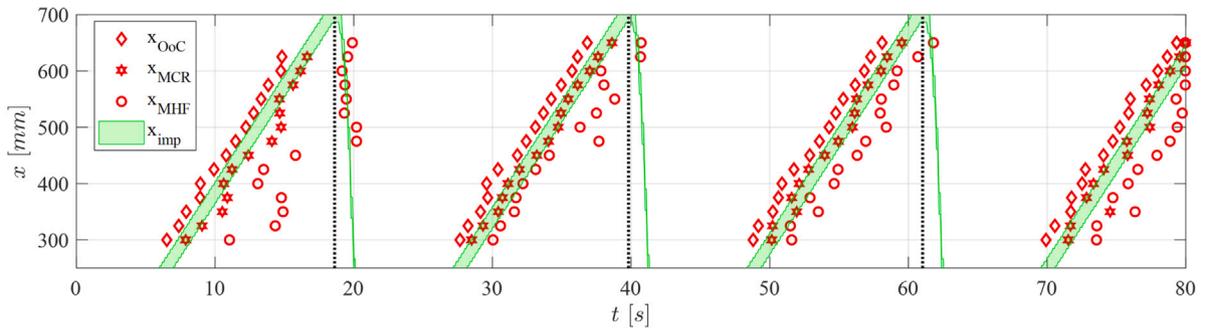
Fig. 8. Test 1 results of the evolution in the cooling key points compared to the 38-mm thick jet impingement region (vertical dotted black lines are the end of each ring pass).

water ring pass, indicating that jet quenching still significantly affects the left side of the sample to the water ring. One possible explanation is that numerous droplets are generated by the jet breakup upon impact with the surface, which fall onto the sample, sustaining the cooling process in this region.

In addition, using the data from 15 thermocouples placed along the sample, we can plot the dissipated heat flux profile along the cylinder axis. Fig. 9 presents this profile for the first three passes of the water jet ring at different times. To assist in understanding the results, arrows are included in the figure to indicate the location of the water jet ring at each instant — arrows pointing left or right denote when the water jet ring is out of the instrumented region. During the first pass, we observe a sharp increase in the dissipated heat flux as the water jet ring reaches the thermocouples, while the dry region, located to the right of the jet ring, shows virtually zero dissipation. In contrast, the wet region, located to the left of the jet ring, displays a fairly constant heat flux profile, indicating a minor influence of the position of the jet ring once the surface has been wetted and cooled. For the second and third passes, a similar sharp increase in dissipated heat flux is observed when the water jet ring passes over the thermocouple locations. However, we also notice that the heat flux profile tends to increase with the x-position. This suggests that regions closer to the water jet ring are experiencing more intense cooling compared to those further away. Nevertheless, this variation is explained by the fact that the surface temperature is lower at smaller x-positions, as illustrated in Fig. 7a. Since heat flux is a function of surface temperature, as we demonstrate next, cooler regions will dissipate less heat compared to hotter regions that are closer to the water jet impact zone, leading to the observed heat flux gradients.

In the last part of analyzing the results from test 1, Fig. 10a shows the boiling curve for each thermocouple, i.e., the dissipated heat flux as a function of the surface temperature. The oscillatory pattern of heat flux with the surface temperature is a consequence of the oscillating temperature evolution and varied cooling conditions for each water ring pass, as observed in Fig. 7, making it difficult to describe any conclusive cooling process behavior from the data. Therefore, we employed two hypotheses to reduce the data and establish a coherent correlation between both the heat flux (Fig. 10b) and the heat transfer coefficient (Fig. 10c) with the surface temperature:

- As highlighted by Gomez et al. [31], significant inaccuracies may arise during the initial stages of the cooling process. Despite confirming the rapid response of our inverse method Appendix and correcting the thermocouple signal for its response time (Section 3.2), there may still be an overestimation of the surface temperature. Hence, for each ring pass, we excluded all data points during the heat flux increase until the midpoint between MCR and MHF, considering them unreliable for correlation. While it might be plausible to consider only the points after the MHF, the time lag between the MCR and the MHF could sometimes persist for several seconds, and both the inverse method and thermocouple correction should be capable of capturing phenomena during this period;
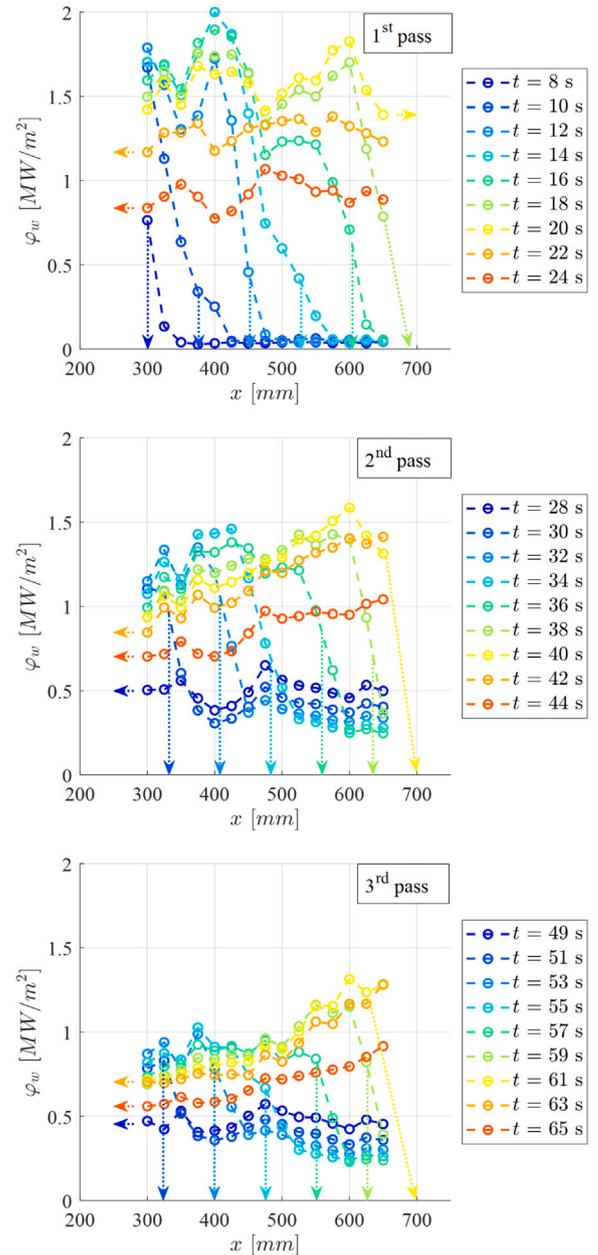

Fig. 9. Test 1 results for the heat flux profile along the cylinder axis for each ring pass. Arrows indicate the water jet ring position — arrows pointing outwards mean the water jet ring is out of the instrumented zone.
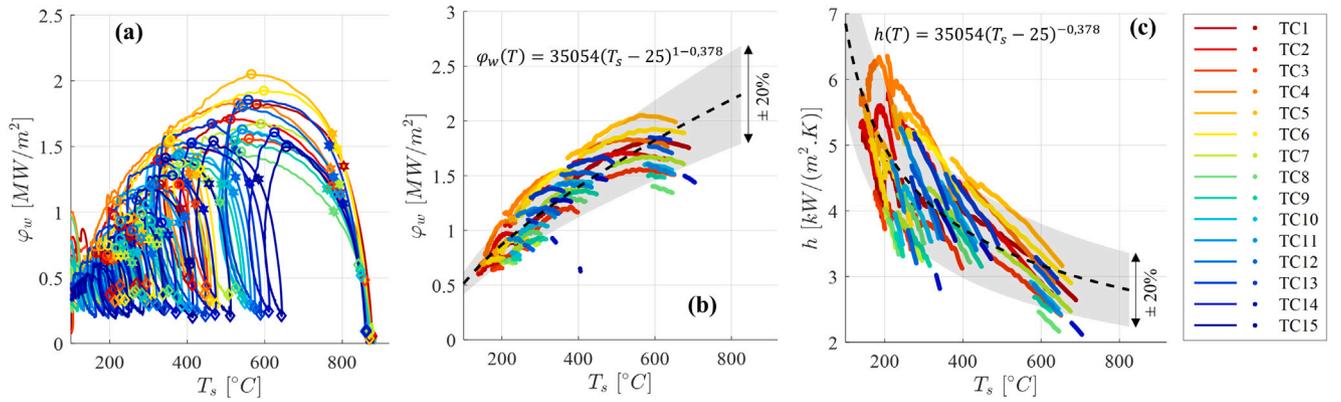
Fig. 10. Test 1 results of boiling curves and heat transfer coefficient at each thermocouple position: (a) boiling curve with all the temperature and estimated heat flux data, including the detected key points (OoC: ⋄, MCR: ☆; MHF: ○); (b) boiling curve with the reduced data, eliminating the beginning of the heat flux growth and during the return of the water jet ring, and the fitted equation (Eq. (12)); (c) estimated heat transfer coefficient with the reduced data and the fitted equation (Eq. (13)).

- The temperature recovery observed in Fig. 7a, along with the corresponding decrease in heat flux shown in Fig. 7b, arises from the experimental setup employed in this study. It was demonstrated that the heat flux remained high while the water ring was still quenching the sample, sharply reducing once the sweeping concluded and the ring returned to the initial position. However, in an actual production line, the steel bar would traverse through several rings spaced by a few dozens of centimeters apart during the cooling process. Consequently, this decrease in heat flux is not representative of an industrial application. Hence, we also disregarded the points between the end of the water ring course and the onset of cooling for the subsequent ring pass.

Hence, Figs. 10b and c present only data points between a midpoint of MCR and MHF for each pass and the end of the corresponding ring pass. A clear correlation between the dissipated heat flux and the surface temperature is now evident: as the surface temperature increases, so does the dissipated heat flux. In fact, we can fit a curve in the form of:

$$\varphi_w(T_s) = C\left(T_s - T_f\right)^{1-n} \tag{12}$$

where C is a proportional factor, T_f is the fluid temperature (25 °C in this study), and $1 - n$ the exponent with an adjusting parameter n. This form was selected so the relation for the heat transfer coefficient h would be:

$$h(T_s) = \frac{\varphi_w(T_s)}{T_s - T_f} = C\left(T_s - T_f\right)^{-n} \tag{13}$$

where $-n$ is the temperature difference exponent. Although the heat transfer coefficient definition (equivalence between Newton's cooling law and Fourier's law in the fluid at the interface) usually implies that the fluid maximum temperature is the same as the wall temperature in a cooling process (which is not the same during film boiling in a quenching process [28,32]), we used directly the wall temperature in Eq. (13) as it provides a global heat transfer coefficient that is useful in numerical heat conduction simulations of the bar cooling process, as we show in Section 5.

An interesting finding is that almost all data points fall within 20% of the adjusted curve regardless of the thermocouple position, indicating that heat dissipation depends only on the surface temperature. This suggests that, for instance, the heat flux dissipation at TC1 is nearly identical to that at TC15 for the same temperature, even though TC15 is directly impacted by the jet, while TC1 is showered by droplets generated by jet shattering on the surface. This highlights the significant cooling effect of the water ring in regions where the water jets are directed, maintaining the quenching process active. Consequently, the heat transfer coefficient behaves uniformly, with virtually all data points falling within 20% of the fitted curve. This uniformity

Table 4
Coefficients and exponents of Eqs. (12) and (13) for each experimental condition.

Test	Q [L/min]	C	n
1	300	35 054	0.378
2	450	16 367	0.231
3	600	27 930	0.325

facilitates modeling quenching processes with water rings, as only a temperature-dependent correlation for the heat transfer coefficient is needed — as done in Appendix to simulate the experiment and validate the inverse method. Notably, the estimated heat transfer coefficients consistently exceed 1500 W/(m²K), surpassing the minimum value found in a previous study for which phase transformations and temperature dependency of properties do not need to be accounted for in the model [7]. In other words, this allows the use of a linear heat conduction equation to estimate the boundary heat flux.

4.2. Water volumetric flow rate effect

We present the reduced data of all 15 thermocouples in Fig. 11a and b for, respectively, the heat flux and the heat transfer coefficient as a function of the surface temperature for different water flow rates. In both graphs, fitted curves for each experiment are also shown, along with the ±20% region for each case. Based on the fitted curves, whose values of C and n are provided in Table 4, we observe an increase in the dissipated heat flux from 300 L/min to 450 L/min (by more than 20% at 800 °C). However, there is a slight reduction for 600 L/min compared to the results for 450 L/min, although it remains higher than the heat flux dissipation for 300 L/min.

One possible explanation for the observed increase and subsequent decrease in heat flux dissipation with increasing water flow rate is the stability of the jet after leaving the nozzle. Analyzing the Ohnesorge diagram in Fig. 12 (the Ohnesorge number being defined as $Oh = \sqrt{We Re^{-1}}$), and the transitions of each jet regime [33], we find that all our test cases fall within the first wind-induced regime, characterized by hydrodynamic instabilities at the interface with no or very few droplet detachment. This contrasts with the second wind-induced regime, observed for higher Reynolds numbers, where increased instability and droplet formation occur before reaching the atomization regime. As the water flow rate increases, the jet regime approaches the second wind-induced regime, leading to greater instability and droplet formation. Notably, the jet is very close to the regime transition for 600 L/min. This was confirmed with lateral-view photos of the water ring jet system used in experiments at ambient temperature (i.e., unheated sample), where 90 photos were captured during 30 s after the water flow rate stabilized. The images in Fig. 12 represent an average of all
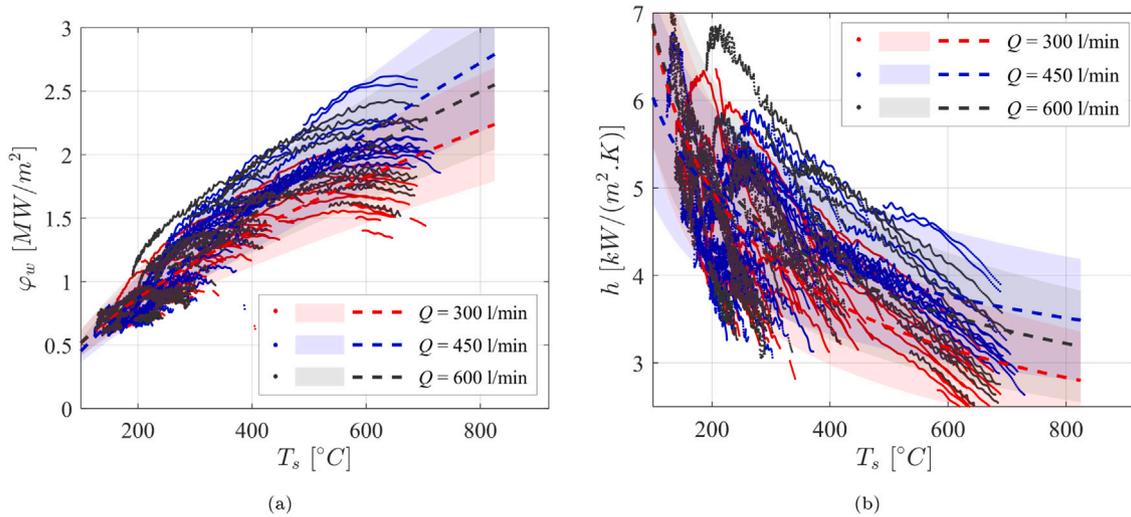
Fig. 11. Effect of the flow rate of the cooling: (a) boiling curve with reduced data, including the fitted equations (Eq. (12)); and (b) estimated heat transfer coefficient with the reduced data and the fitted equations (Eq. (13)).

the pictures, providing insight into the average behavior for each flow rate.

Analyzing the angles after jet impingement on the cold sample reveals that the tested flow rates produce consistent results. It can be seen that gravity impacts the jets (bottom angle slightly larger than top angle) but this effect was verified to be similar for the three tested water flow rates. However, examining the jet exit at the nozzle (indicated by yellow arrows), we observe a more well-behaved jet for 300 L/min and 450 L/min compared to 600 L/min, where a thicker, foggy jet is visible immediately after the nozzle. This observation suggests the formation of small droplets as the jet condition approaches the second wind-induced regime. Consequently, at the flow rate of 600 L/min, some of the liquid intended to impact the steel bar during the cooling process may not reach the sample surface due to droplet formation, which cannot effectively impact the surface like the jet itself. This demonstrates that, for jet quenching systems, an increase in flow rate may not necessarily translate to increased cooling capacity, as changes in the jet regime can degrade heat transfer efficiency.

Fig. 13 illustrates the behavior of cooling key points for different water flow rates compared to the water ring impingement region. To ensure clarity of the graph, only points for selected thermocouple locations are presented. As observed in test 1 (Fig. 8), the onset of cooling points precedes slightly the arrival of the water jet at the location, the maximum cooling rate occurs within the impingement region, and the maximum heat flux occurs shortly after the water jet ring has passed. This consistent behavior was observed across all the tested water flow rates. The results of the maximum heat flux point for the first ring pass is another evidence of the improved cooling for 450 L/min compared to the other flow rates. For 450 L/min (blue circles), the maximum heat flux is reached immediately after the water jet ring passes, except at the last thermocouple position. In contrast, for 300 L/min and 600 L/min (red and black circles, respectively), the maximum heat flux is reached only at the end of the water jet ring sweeping, during its return to the start point, from TC15 to TC9. This indicates that only at 450 L/min the system was capable of cooling the bar rapidly enough to reach the maximum heat flux during the quenching process. On the other hand, for the other water flow rates, the heat flux growth was interrupted by the end of the water jet ring sweeping course.

Finally, we compare in Fig. 14 the cooling curves for two flow rates – 300 L/min and 600 L/min – for the second instrumentation shown in Fig. 2, with TC3 located at the center of the bar. Both cooling curves exhibit a similar trend for both water flow rates. Particularly for the first two thermocouples, the cooling curves are very similar, with a
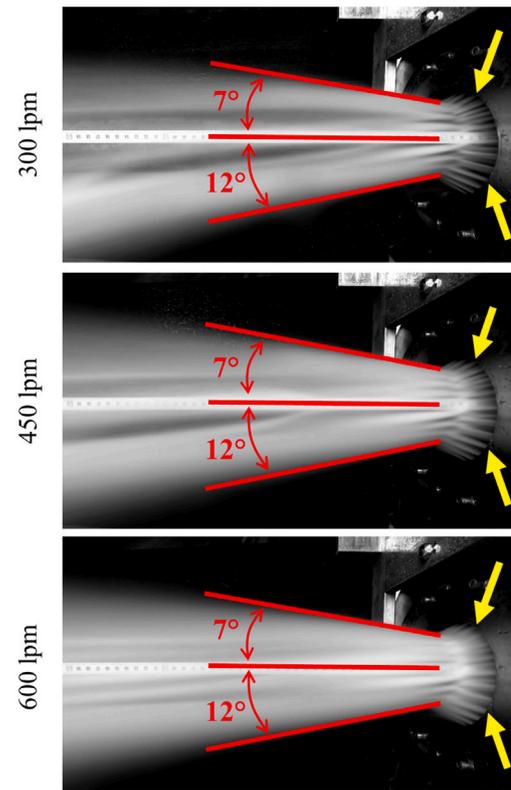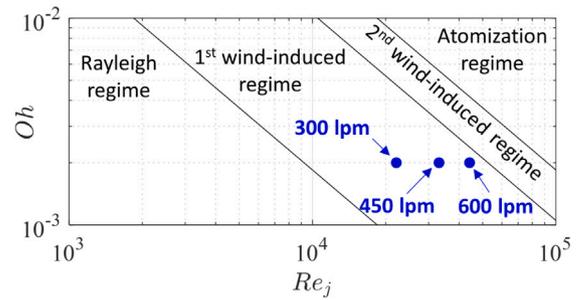

Fig. 12. Ohnesorge diagram and pictures of the jet visualization tests at ambient temperature, including the angles of the splashed water after impacting the surface. Yellow arrows indicate the jet at the exit of the nozzles to compare the difference in each flow rate.
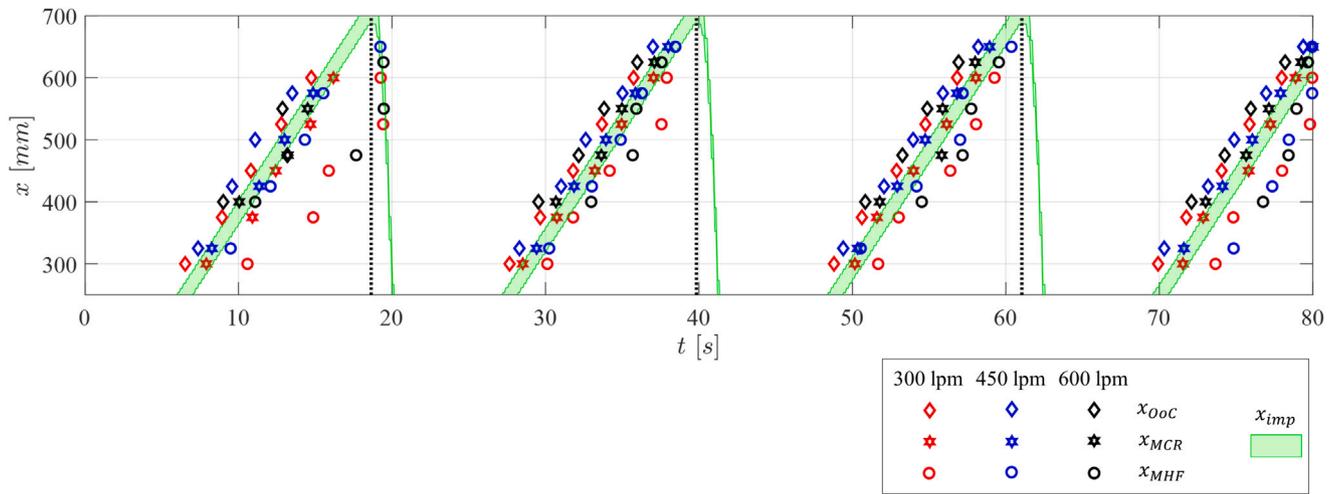
Fig. 13. Cooling key points evolution for different water flow rates compared to the jet impingement region.
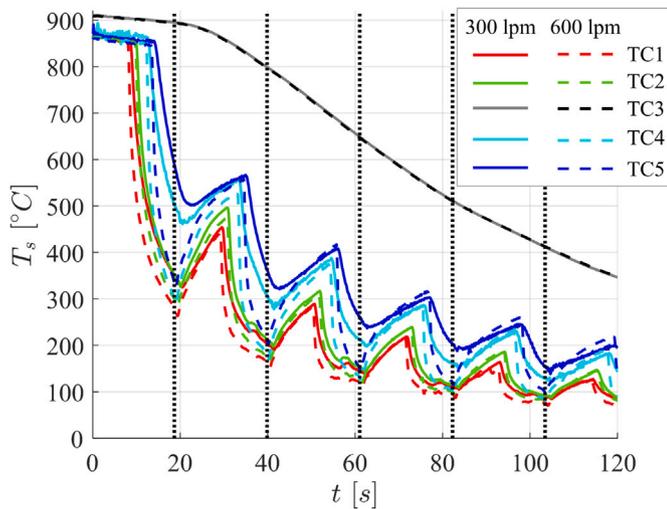

Fig. 14. Temperature evolution results for two tests with different flow rates, including a measurement at the center of the bar (TC3).

slightly higher cooling rate observed for the results with 600 L/min. However, a larger difference between the two flow rates is observed for TC4 and TC5 measurements. This discrepancy could potentially be attributed to an instrumentation issue for 600 L/min, such as water intrusion in the holes leading to a reduction in the measured temperature. One supporting indication for this hypothesis is the rapid convergence of TC4 and TC5 measurements to the same value in the recovery region for both 300 L/min and 600 L/min, suggesting that water in the holes may have evaporated, allowing these thermocouples to measure the surface temperature correctly again. It is noteworthy that TC1 and TC2 measurements follow a similar trend in the recovery region for both flow rates. Furthermore, another indication of similar cooling capacities for both flow rates is the TC3 measurement at the center of the bar. After two minutes of cooling and six water ring passes, the core temperature difference between the two tests is only 2 °C, indicating virtually no difference in the dissipated heat flux between the two cases. This finding confirms the minor effect of water flow rates for the tested conditions near industrial scale.

5. Industrial condition simulation

The goal of this numerical part is to use the heat transfer coefficient (h) expression defined by the inverse method (Eq. (13)) to simulate the

quenching experiments of the present study in test 1 condition, i.e. with 300 L/min, using a 3D model developed in FORGE NxT 4.0®. FORGE® is a software solution commercialized by Transvalor for simulating hot and cold forming processes, among other applications. This code utilizes the finite element (FE) method and use a metallurgical database to perform the thermal and phase transformations coupling, which enables to predict the amount of crystallographic phases formed during heat treatment and quenching — for example, how much austenite was converted into martensite.

Fig. 15 illustrates the bar and a schematic view of the water jet ring, which is not included in the calculation but shown for its relative position to the bar. The bar is discretized with a very refined mesh at the surface where heat extraction occurs, using a tetrahedron mesh with a 1 mm side. To optimize computation time, only 1/8 of the 3D bar is modeled, employing two planes of symmetry with adiabatic thermal conditions. Sensors are positioned according to the locations of thermocouples (Fig. 15) in the model to record temperatures as a function of time.

In this model, unlike the experimental tests, the ring is fixed and the bar translates through the ring without rotation. Initially, the bar temperature is homogeneous at 920 °C. The cooling of the bar is controlled by the coefficient h (for a flow rate of 300 L/min), imposed on the surface. The heat transfer coefficient can depend on the surface temperature of the bar, its position compared to the jet impact location, and time, as described in Eq. (A.6). Concerning the material data of the bar, the thermophysical properties depend on temperature. When metallurgical transformations are considered, these properties also depend on the phases. The kinetics of phase transformations and the thermophysical properties are included in the software database for 35MnCrMoV5 steel.

Fig. 16 shows the temperature at the position of the second thermocouple (TC2), i.e. about 2 mm below the surface of the bar, as a function of time during the first three quenches from three different results: (1) thermocouple measurements from test 1 (solid black line); (2) using the estimated heat flux by the inverse method and simulating the thermocouple measurement using a linear heat conduction model (Eq. (10), dotted green line); and (3) FE simulations with FORGE, which also uses the estimated heat flux by the inverse method but one includes metallurgical transformations (dashed red line) while the other neglects it (dash-dotted blue line). The three quenches are easily identified by a sharp drop in temperature. After each quenching, there is a temperature rise due to the return of the ring to its starting point. Overall, we observe a good correlation between the measurements, linear model calculations, and FE simulations. The difference between experimental and simulated data during the first quenching is partially attributed to the thermocouple response time, as discussed in Section 3.2, which is
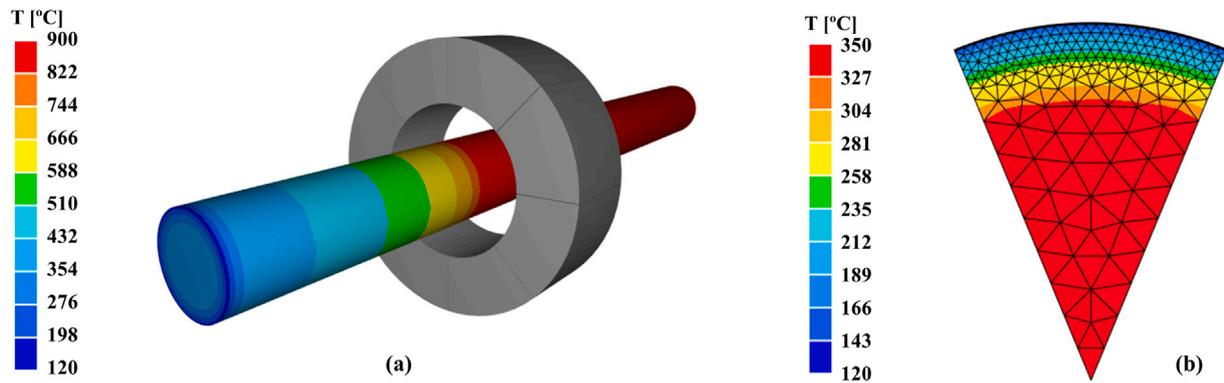
Fig. 15. Finite element model with FORGE NxT 4.0®: (a) 3D model with the bar and the ring; (b) bar mesh (cutting plane at the front face).
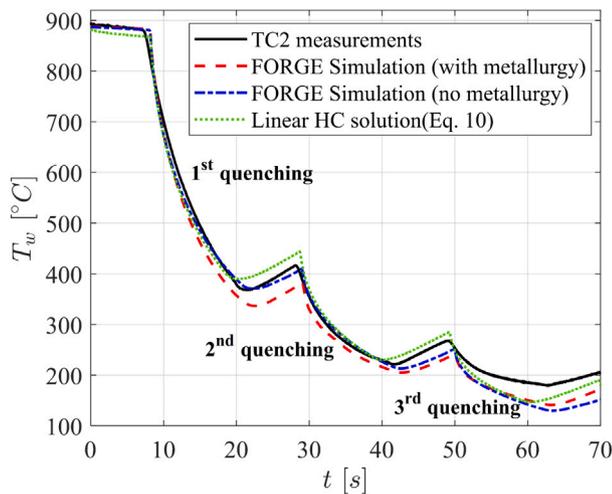

Fig. 16. Comparison between measurements from test 1 and temperature estimates using the estimated heat flux by the inverse method, one result from the linear heat conduction model (Eq. (10)) and two results from FE simulations with and without metallurgical transformations.

not considered in the calculations. At the end of the third quenching, inverse method calculations and FE simulations yield almost identical results, with only a slight discrepancy of 25 °C compared to the thermocouple data. This indicates that the expression for *h* works well, even when metallurgical transformations are considered, which confirms the statement made by Oliveira et al. [7] that phase transformation phenomena can be neglected in fast cooling processes to estimate the boundary heat flux.

Ascometal has an induction heat treatment line for bars, which includes a 4-meter-long quenching zone (Fig. 17). At the entrance and exit of this area, two pyrometers measure the surface temperature of the bars — normally, the bar enters at 890 °C and at leaves the quenching zone at 60 °C when all the cooling system are operating. The quenching zone contains four water jet rings (the same as the one used in the experimental apparatus). The bar translation and rotation are driven by drive rollers. The area occupied by the water jet rings is relatively small, but the jet wake after the impact location can still impinge the bar, as shown in Fig. 12, thereby creating a "wet" zone of approximately 2.7 m.

Tests in the production line of a 57-mm-diameter bar quenching with a water flow rate of 720 L/min in each water jet ring show that the bar leaves the quenching zone at approximately 60 °C. We performed FE simulations (with FORGE®, including metallurgical transformations) of the bar cooling process using the expression for *h* in Eq. (A.6) but using *C* and *n* for 600 L/min (Table 4), which is the highest water

flow rate data available. Fig. 18 shows the simulation results along the quenching zone as temperatures at surface, half-radius and center of the bar. The impact of the four water jet rings is clearly visible on the surface, with a temperature drop of more than 800 °C. The minimum surface temperature is about 65 °C at the end of the water rings effect. Then the center of the bar reheats the surface by conduction to reach a surface temperature of 140 °C at the exit of the quenching zone, while the pyrometer measures 60 °C. This +80 °C difference is partially a result of the internal heat source that was neglected in the linear inverse model, as reported by Oliveira et al. [7]. In fact, this result corroborates their conclusion: phase transformation phenomena can be neglected for sufficiently accurate estimates of the boundary heat flux, but it can lead to a small bias when re-estimating the sample temperature using the estimated heat flux — or, in this case, the estimated heat transfer coefficient correlation.

It should be noted that our large-scale cooling experimental bench contains only one ring, without drive rollers and casing. All these factors may have a significant impact on the water jet behavior, as the rings are relatively close to each other. Therefore, it would be interesting in future experiments to test the impact of a second ring in a near-industrial scale experimental bench as used in this study.

6. Conclusions

This paper presents the results of steel bar cooling under near-industrial conditions and investigates the influence of water flow rate on the cooling process. Employing a water jet ring system with 120 jets, the study emulates a steel production line scenario where a bar traverses multiple water jet rings. Utilizing 15 thermocouple measurements, the dissipated heat flux is estimated via a pseudo-analytical inverse method, while important cooling key points — the onset of cooling (OoC), maximum cooling rate (MCR), and maximum heat flux (MHF) – are determined from experimental data. Signal correction of the thermocouples, accounting for their response time, improves the accuracy of surface temperature and dissipated heat flux estimates along the bar.

A detailed analysis of a single test (test 1) reveals that the data processing effectively captures the cooling key points, consistently occurring in a specific order: OoC precedes the water jet's arrival, MCR coincides with the impingement region, and MHF occurs at – or slightly after – the water jet passage. Notably, MHF occasionally takes place during the water jet ring's return to the start position due to premature interruption of heat flux growth. Subsequently, a data elimination method is proposed to avoid misinterpretation of the inverse method results and to exclude data during the water jet ring's return, ensuring a representative analysis of the industrial process. This allows the observation of a clear correlation between surface temperature and dissipated heat flux, represented by a fitted equation $\varphi_w(T_s) = C(T_s - T_f)^{1-n}$, with nearly all experimental data falling within ±20%
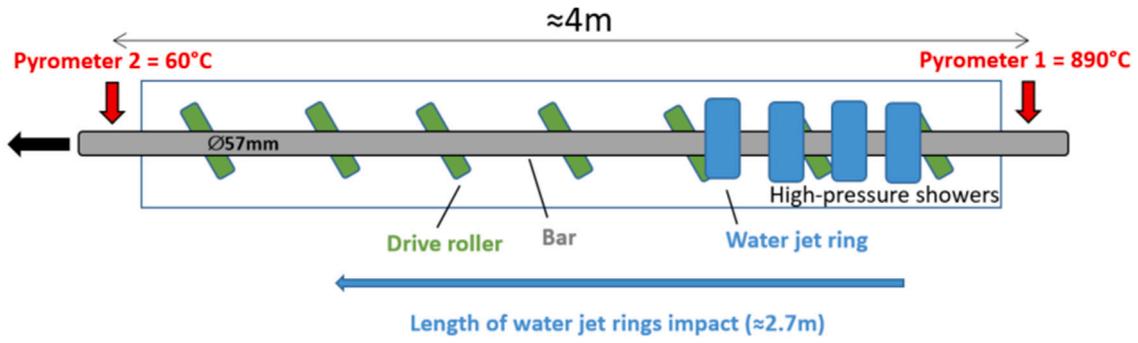
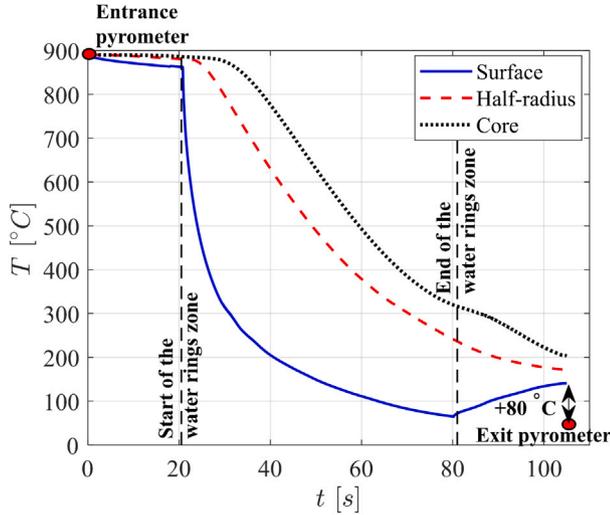**Fig. 17.** Industrial water quenching zone.

Fig. 18. Temperature from the FE simulation of the induction line quenching.

of the fitted curve. Consequently, the heat transfer coefficient can also be correlated with surface temperature using $h(T_s) = C(T_s - T_f)^{-n}$. Interestingly, results indicate that dissipated heat flux and heat transfer coefficient remain independent of thermocouple position relative to the water jet ring, provided the thermocouple is within the wet area.

Furthermore, the paper examines the effect of water flow rate, revealing no significant impact under the tested conditions. A slight increase in dissipated heat flux is observed with flow rate elevation from 300 L/min to 450 L/min, followed by a marginal decrease at 600 L/min. This phenomenon may be attributed to increased hydrodynamic instabilities at 600 L/min, resulting in droplet formation that cannot attain surface contact during jet cooling, thereby reducing heat dissipation efficiency. This minor influence of water flow rate is confirmed through core temperature measurements, where doubling the flow rate from 300 L/min to 600 L/min yields practically no difference in core temperatures. Thus, under near-industrial conditions, increasing water flow rate does not necessarily translate to higher dissipated heat flux. Finally, we performed numerical simulations considering metallurgical phenomena, using the proposed correlation for the heat transfer coefficient in industrial conditions, and the results are satisfactory considering the heat flux was estimated using a linear inverse heat conduction model, experimentally confirming the conclusions of a previous study that phase transformations can be neglected in fast cooling processes for heat flux estimation.

CRediT authorship contribution statement

A.V.S. Oliveira: Methodology, Data curation, Software, Investigation, Writing – original draft. **D. Maréchal:** Methodology, Data

curation, Investigation, Project administration, Writing – review & editing. **D. Lawrjaniec:** Methodology, Data curation, Software, Investigation, Writing – original draft. **M. Gradeck:** Conceptualization, Supervision, Methodology, Writing – review & editing.

Declaration of competing interest

The authors declare that they have no known competing financial interests or personal relationships that could have appeared to influence the work reported in this paper.

Appendix. Assessing the quality of the inverse method estimation

We evaluated the accuracy of heat flux estimation by employing pseudo-analytical techniques to solve the two-dimensional heat conduction equation (Eq. (3)). This involved applying a temperature-dependent heat flux function at the boundary $r = R$. By employing Laplace and Fourier cosine transforms, we derived an ordinary differential equation, which can be expressed as:

$$\frac{\partial^2 \widetilde{\widetilde{\theta}}_n}{\partial r^2} + \frac{1}{r}\frac{\partial \widetilde{\widetilde{\theta}}_n}{\partial r} - \left(\frac{p}{a} + \omega_n^2\right)\widetilde{\widetilde{\theta}}_n = 0 \tag{A.1}$$

where $(\widetilde{\cdot})$ corresponds to a variable in the Fourier space — hence, $\widetilde{\widetilde{\theta}}_n$ means temperature in both Laplace and Fourier spaces for the harmonic n. Considering the boundary conditions in the r-direction (symmetry at the center and φ_w heat flux at the surface), the solution for this equation is:

$$\widetilde{\widetilde{\theta}}_n = -\frac{1}{\lambda}\frac{I_0\left(\sqrt{\frac{p+\omega_n^2\alpha}{\alpha}}r\right)}{\sqrt{\frac{p+\omega_n^2\alpha}{\alpha}}I_1\left(\sqrt{\frac{p+\omega_n^2\alpha}{\alpha}}R\right)}\widetilde{\widetilde{\varphi}}_{w,n} \tag{A.2}$$

where $\omega_n = n\pi/L$ for $n = 0, 1, 2...$ and L the cylinder's length. The solution of the inverse Laplace transform is:

$$\widetilde{\theta}_n(r,t) = -\frac{1}{\lambda}\int_0^t \widetilde{\varphi}_{w,n}(t)\left[\exp^{-\omega_n^2\alpha(t-\tau)}Z(r,t-\tau)\right]d\tau \tag{A.3}$$

so, we can calculate the temperature difference harmonics $\widetilde{\theta}_n(r,t)$ discretely using Duhamel's theorem as follows:

$$\widetilde{\theta}_n(r,t_k) = \sum_{m=0}^{k-1}X(r,t_k-t_m)\widetilde{\varphi}_{w,n}(t_k) \tag{A.4}$$

X being:

$$X(r, t_k) = -\frac{1}{\lambda} \int_{t_k}^{t_{k+1}} \exp^{-\omega_n^2 \alpha \tau} Z(r, \tau) d\tau \qquad (A.5)$$

and Z being also the same as given in Eq. (9).

The validation of the inverse method was performed using the results of test 1, which gave the following expression for $\varphi_w(T)$:

$$\varphi_w(T) = \begin{cases} 35054(T_s - 25)^{1-0.378} & , \text{ if } x_{TC} \leq x_{ring} \\ \quad \text{for any ring pass (wet area)} \\ 8(T_s - 25) + \varepsilon\sigma\left[(T_s + 273)^4 - 298^4\right] & , \text{ if } x_{TC} > x_{ring} \\ \quad \text{for the first ring pass (dry area)} \\ 35054\left[T_s(t_{end}) - 25\right]^{1-0.378} exp\left(-\frac{t-t_{end}}{t_d}\right) & , \text{ if } x_{TC} > x_{ring} \\ \quad \text{for the other ring passes (recovery area)} \end{cases}$$

$$(A.6)$$

the first expression corresponds to the heat flux estimated from the test results (Fig. 10), the second expression represents the dry area where heat dissipation occurs primarily through free convection and radiation (here, we fixed the heat transfer coefficient at 8 W/(m²K) and the emissivity at $\varepsilon = 0.5$, parameters determined to fit the experimental data), and the third expression describes the recovery area when the water jet ring returns to the start point, characterized by a time constant $t_d = 7$ s (Fig. 7), with t_{end} denoting the time when the water jet ring completes its sweep for a given pass. This third condition is required to simulate the back-and-forth movement of the ring; however, it does not apply to a metallurgical process where the product passes along multiple rings.

Fig. A.19 displays the results of the direct problem simulation, where Eq. (A.6) is imposed as boundary condition. The filled lines represent the simulated temperature response, while the dashed lines in the top plot depict the estimated heat flux using simulated thermocouple measurements to infer the boundary heat flux at each thermocouple location. Circular symbols represent the corresponding experimental results obtained for test 1, serving as a comparison. In the top plot, the evolution of heat flux above four different thermocouples is illustrated, while the bottom plot shows temperature measurements and simulations for the same thermocouples, with the dashed black line indicating the jet impact location x_{ring} as a reference.

Overall, the proposed boundary condition in Eq. (A.6) effectively captures the cooling dynamics observed in test 1, including rapid cooling upon the water ring's arrival at the thermocouple location and subsequent temperature recovery upon its return to the start point. Therefore, this simulation is representative of the test conditions, serving as a means to assess the quality of the inverse method. Despite some noise in the estimated heat flux, it remains negligible compared to the heat flux magnitude. Specifically, the error in the estimates (difference between estimation and imposed values) consistently remains below 0.1 MW/m² for heat fluxes exceeding 0.5 MW/m² (Fig. A.20).

Particularly in the experiment conducted in this study, estimating the boundary heat flux presents challenges due to significant variations in both time and space at the surface of the bar. While rapid transients can be captured by increasing the data acquisition rate, accurately estimating steep spatial gradients is more challenging. This would necessitate a larger number of thermocouples positioned very closely together to enable the use of more Fourier harmonics for solving the full heat equation (Eq. (3)) and describing the heat flux profile at each time step.

Upon comparing the quality of heat flux estimates using both a two-dimensional heat conduction model, as done in a previous work on single-jet flat plate cooling [19], and a one-dimensional model as presented in Section 3.1, we observed that the one-dimensional approach provided more accurate and stable results. The two-dimensional approach was notably affected by oscillations in the Fourier harmonics,
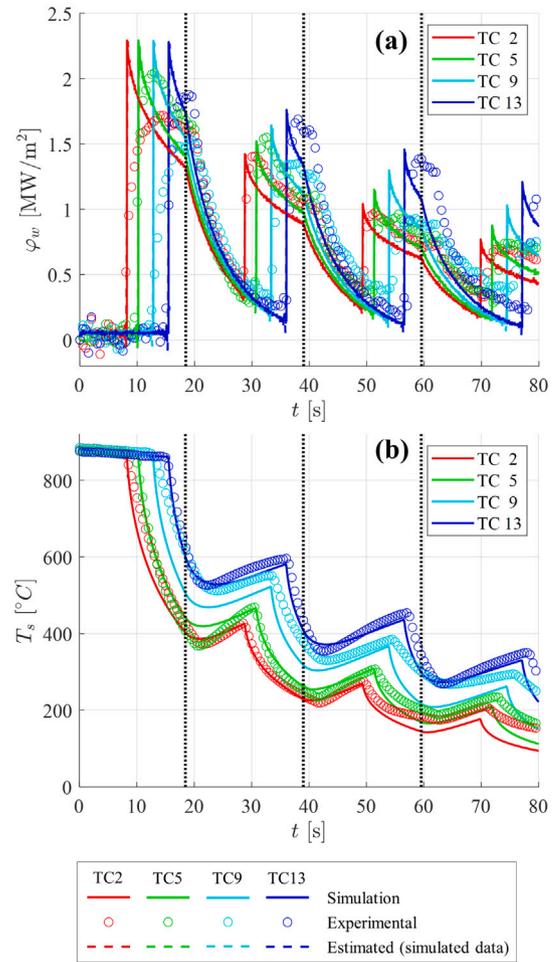

Fig. A.19. Comparison between simulation and experimental results at some thermocouple positions: (a) boundary heat flux, showing imposed and estimated values in the simulation and experimental data (test 1); (b) simulated and measured temperature evolutions. The dotted black lines represent the instant the water ring returns to its initial position.
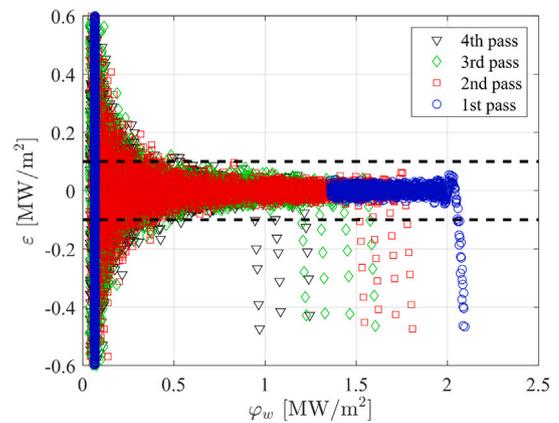

Fig. A.20. Error in the heat flux estimate as a function of the boundary heat flux value for each simulated ring pass.

as illustrated in Fig. A.21. This suggests that radial heat conduction is significantly predominant over axial heat conduction when the jet ring passes over the thermocouple location. Given this observation, we opted to employ the one-dimensional model for the inverse method.
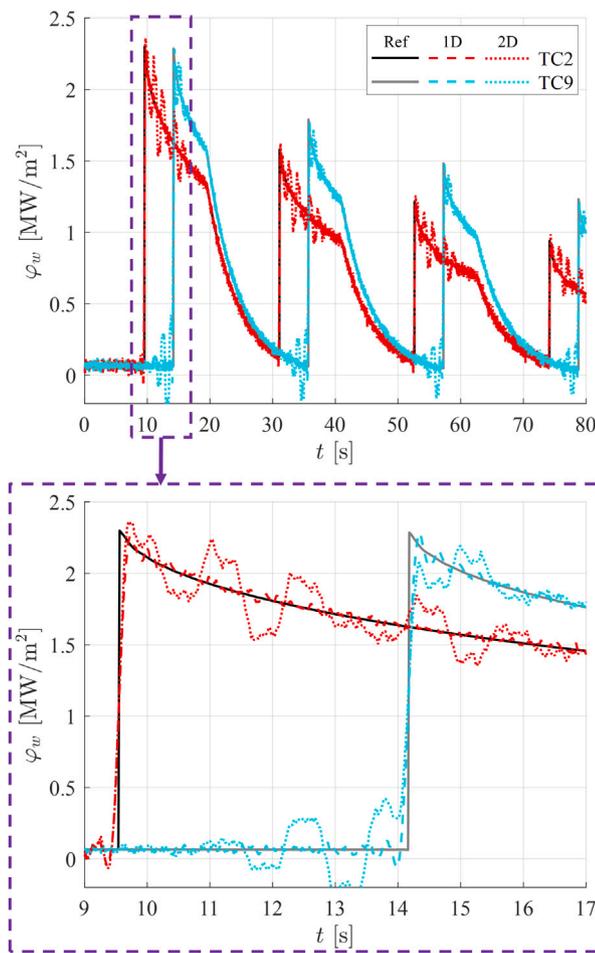
Fig. A.21. Comparison between the heat flux estimates using one- and two-dimensional heat conduction models in the inverse method.

Data availability

The authors do not have permission to share data.

References

[1] B. Li, T. Cader, J. Schwarzkopf, K. Okamoto, B. Ramaprian, Spray angle effect during spray cooling of microelectronics: Experimental measurements and comparison with inverse calculations, Appl. Therm. Eng. 26 (16) (2006) 1788–1795, http://dx.doi.org/10.1016/j.applthermaleng.2006.01.023.

[2] S.M. Ammar, C.W. Park, Evaporation heat transfer characteristics of falling film in small diameter fabricated tubes of absorption refrigeration system: An experimental investigation, Int. J. Heat Mass Transfer 165 (2021) 120618, http://dx.doi.org/10.1016/j.ijheatmasstransfer.2020.120618.

[3] D.C. Moreira, V.S. Nascimento, G. Ribatski, S.G. Kandlikar, Combining liquid inertia and evaporation momentum forces to achieve flow boiling inversion and performance enhancement in asymmetric dual V-groove microchannels, Int. J. Heat Mass Transfer 194 (2022) 123009, http://dx.doi.org/10.1016/j.ijheatmasstransfer.2022.123009.

[4] S. Mori, N. Maruoka, K. Okuyama, Critical heat flux enhancement by a two-layer structured honeycomb porous plate in a saturated pool boiling of water, Int. J. Heat Mass Transfer 118 (2018) 429–438, http://dx.doi.org/10.1016/j.ijheatmasstransfer.2017.10.100.

[5] A.V.S. Oliveira, J.D. Peña Carrillo, A. Labergue, T. Glantz, M. Gradeck, Experimental study of dispersed flow film boiling at sub-channel scale in LOCA conditions: Influence of the steam flow rate and residual power, Appl. Therm. Eng. 172 (2020) 115143, http://dx.doi.org/10.1016/j.applthermaleng.2020.115143.

[6] A.K. Mozumder, M. Ahmed, Jet quenching phenomena during emergency cooling of high temperature solid surface, Energy Procedia 160 (2019) 356–363,

[7] http://dx.doi.org/10.1016/j.egypro.2019.02.168, 2nd International Conference on Energy and Power, ICEP2018, 13–15 December 2018, Sydney, Australia.

[7] A.V.S. Oliveira, J. Teixeira, V. Schick, D. Maréchal, M. Gradeck, S. Denis, Using a linear inverse heat conduction model to estimate the boundary heat flux with a material undergoing phase transformation, Appl. Therm. Eng. 219 (2023) 119406, http://dx.doi.org/10.1016/j.applthermaleng.2022.119406.

[8] G. Liang, I. Mudawar, Review of spray cooling – Part 2: High temperature boiling regimes and quenching applications, Int. J. Heat Mass Transfer 115 (2017) 1206–1222, http://dx.doi.org/10.1016/j.ijheatmasstransfer.2017.06.022.

[9] H. Leocadio, C.W.M. van der Geld, J.C. Passos, Rewetting and boiling in jet impingement on high temperature steel surface, Phys. Fluids 30 (12) (2018) 122102, http://dx.doi.org/10.1063/1.5054870.

[10] N. Karwa, P. Stephan, Experimental investigation of free-surface jet impingement quenching process, Int. J. Heat Mass Transfer 64 (2013) 1118–1126, http://dx.doi.org/10.1016/j.ijheatmasstransfer.2013.05.014.

[11] C. Gomez, C. van der Geld, J. Kuerten, M. Bsibsi, B. van Esch, Quench cooling of fast moving steel plates by water jet impingement, Int. J. Heat Mass Transfer 163 (2020) 120545, http://dx.doi.org/10.1016/j.ijheatmasstransfer.2020.120545.

[12] G.G. Guemo, A.H. Nobari, V. Prodanovic, M. Militzer, Modeling transient jet impingement cooling of moving hot steel plates, ISIJ Int. 62 (11) (2022) 2331–2342, http://dx.doi.org/10.2355/isijinternational.ISIJINT-2021-457.

[13] A.K. Mozumder, Y. Mitsutake, M. Monde, Subcooled water jet quenching phenomena for a high temperature rotating cylinder, Int. J. Heat Mass Transfer 68 (2014) 466–478, http://dx.doi.org/10.1016/j.ijheatmasstransfer.2013.09.059.

[14] S. Devynck, S. Denis, J.P. Bellot, T. Benard, M. Gradeck, Influence of boiling heat transfer and phase transformations on the deformation of a steel tube during quenching by impinging water jets, Mater.wiss. Werkst.tech. 47 (2016) 755–761, http://dx.doi.org/10.1002/mawe.201600609.

[15] M. Gradeck, A. Kouachi, M. Lebouché, F. Volle, D. Maillet, J. Borean, Boiling curves in relation to quenching of a high temperature moving surface with liquid jet impingement, Int. J. Heat Mass Transfer 52 (5) (2009) 1094–1104, http://dx.doi.org/10.1016/j.ijheatmasstransfer.2008.09.015.

[16] M. Jahedi, B. Moshfegh, Quenching a rotary hollow cylinder by multiple configurations of water-impinging jets, Int. J. Heat Mass Transfer 137 (2019) 124–137, http://dx.doi.org/10.1016/j.ijheatmasstransfer.2019.03.066.

[17] C. Agrawal, R. Kumar, A. Gupta, B. Chatterjee, Rewetting of hot vertical rod during jet impingement surface cooling, Heat Mass Transf. 52 (2016) 1203–1217, http://dx.doi.org/10.1007/s00231-015-1637-9.

[18] K. Baghel, A. Sridharan, J.S. Murallidharan, Heat transfer characteristics of free surface water jet impingement on a curved surface, Int. J. Heat Mass Transfer 164 (2021) 120487, http://dx.doi.org/10.1016/j.ijheatmasstransfer.2020.120487.

[19] A.V.S. Oliveira, D. Maréchal, J.-L. Borean, V. Schick, J. Teixeira, S. Denis, M. Gradeck, Experimental study of the heat transfer of single-jet impingement cooling onto a large heated plate near industrial conditions, Int. J. Heat Mass Transfer 184 (2022) 121998, http://dx.doi.org/10.1016/j.ijheatmasstransfer.2021.121998.

[20] M. Chabicovsky, J. Horsky, M. Raudensky, M. Hnizdil, P. Kotrbacek, Design of quenching units for heat treatment of tubes, La Metallurgia Ital. 10 (2015) 31–36.

[21] R. Zhang, Z. Li, Y. Zhang, D. Chen, G. Yuan, Numerical investigation of jet layout for annular jet cooling on a steel tube, Appl. Therm. Eng. 213 (2022) 118825, http://dx.doi.org/10.1016/j.applthermaleng.2022.118825.

[22] G. Yuan, R. Zhang, Y. Zhang, J. Kang, Z. Li, X. Liu, J. Wang, Heat transfer characteristics of a hot-rolled seamless steel tube during a controlled cooling process, Steel Res. Int. 94 (2023) 2200150, http://dx.doi.org/10.1002/srin.202200150.

[23] M.N. Özişik, Heat Conduction, in: Wiley-Interscience Publication, John Wiley & Sons, 1993.

[24] H. Stehfest, Algorithm 368: Numerical inversion of Laplace transforms [D5], Commun. ACM 13 (1) (1970) 47–49, http://dx.doi.org/10.1145/361953.361969.

[25] J.V. Beck, B. Blackwell, C.R. St. Clair Jr., Inverse Heat Conduction: Ill-Posed Problems, in: Wiley-Interscience Publication, John Wiley & Sons, 1985.

[26] P. Le Masson, T. Loulou, E. Artioukhine, P. Rogeon, D. Carron, J.-J. Quemener, A numerical study for the estimation of a convection heat transfer coefficient during a metallurgical "Jominy end-quench" test, Int. J. Therm. Sci. 41 (6) (2002) 517–527, http://dx.doi.org/10.1016/S1290-0729(02)01345-5.

[27] A.V.S. Oliveira, A. Avrit, M. Gradeck, Thermocouple response time estimation and temperature signal correction for an accurate heat flux calculation in inverse heat conduction problems, Int. J. Heat Mass Transfer 185 (2022) 122398, http://dx.doi.org/10.1016/j.ijheatmasstransfer.2021.122398.

[28] K. Tsukamoto, Y. Kita, S. Inoue, T. Hamanosono, S. Hidaka, S. Ueoka, H. Fukuda, M. Kohno, Y. Takata, On the onset of quench during spray cooling: The significance of oxide layers, Appl. Therm. Eng. 179 (2020) 115682, http://dx.doi.org/10.1016/j.applthermaleng.2020.115682.

[29] J.H. Lienhard V, J.H. Lienhard IV, A Heat Transfer Textbook, sixth ed., Phlogiston Press, Cambridge, MA, 2024, Version 6.00. URL https://ahtt.mit.edu.

[30] V.V. Yagov, K.B. Minko, A.R. Zabirov, Two distinctly different modes of cooling high-temperature bodies in subcooled liquids, Int. J. Heat Mass Transfer 167 (2021) 120838, http://dx.doi.org/10.1016/j.ijheatmasstransfer.2020.120838.

[31] C.F. Gomez, R. Nieuwenhuizen, C.W. van der Geld, H.G. Kuerten, M. Bsibsi, B.P. van Esch, Inaccuracies in the inverse heat conduction problem solution and their effect on the estimation of heat fluxes during quenching, Int. J. Heat Mass Transfer 194 (2022) 122953, http://dx.doi.org/10.1016/j.ijheatmasstransfer.2022.122953.

[32] E. Specht, Heat and Mass Transfer in Thermoprocessing: Fundamentals, Calculations, Processes, in: Edition Heat Processing, Vulkan Verlag, 2017.

[33] S.P. Lin, R.D. Reitz, Drop and spray formation from a liquid jet, Annu. Rev. Fluid Mech. 30 (1) (1998) 85–105, http://dx.doi.org/10.1146/annurev.fluid.30.1.85.